AUTHOR QUERY FORM

ELSEVIER	**Journal: SCT** **Article Number: 16793**	**Please e-mail or fax your responses and any corrections to:** **E-mail: corrections.esil@elsevier.spitech.com** **Fax: +1 619 699 6721**

Dear Author,

Any queries or remarks that have arisen during the processing of your manuscript are listed below and highlighted by flags in the proof. Please check your proof carefully and mark all corrections at the appropriate place in the proof (e.g., by using on-screen annotation in the PDF file) or compile them in a separate list.

For correction or revision of any artwork, please consult http://www.elsevier.com/artworkinstructions.

Any queries or remarks that have arisen during the processing of your manuscript are listed below and highlighted by flags in the proof. Click on the 'Q' link to go to the location in the proof.

Location in article	**Query / Remark: click on the Q link to go** **Please insert your reply or correction at the corresponding line in the proof**
Q1	Please check the telephone/fax number of the corresponding author, and correct if necessary.

Thank you for your assistance.

Surface & Coatings Technology xxx (2011) xxx

Contents lists available at ScienceDirect

Surface & Coatings Technology

journal homepage: www.elsevier.com/locate/surfcoat

Highlights

Surface & Coatings Technology xxx (2011) xxx–xxx

A comparison between fine-grained and nanocrystalline electrodeposited Cu–Ni films. Insights on mechanical and corrosion performance

E. Pellicer [a,*], A. Varea [a], S. Pané [b], K.M. Sivaraman [b], B.J. Nelson [b], S. Suriñach [a], M.D. Baró [a], J. Sort [c]

[a] *Departament de Física, Facultat de Ciències, Universitat Autònoma de Barcelona, E-08193 Bellaterra, Spain*
[b] *Institute of Robotics and Intelligent Systems (IRIS), ETH Zurich, CH-8092 Zurich, Switzerland*
[c] *Institució Catalana de Recerca i Estudis Avançats (ICREA) and Departament de Física, Universitat Autònoma de Barcelona, E-08193 Bellaterra, Spain*

► Fine-grained and nanocrystalline electrodeposited Cu–Ni alloy films. ► The nanocrystalline films perform mechanically better than the fine-grained ones. ► The nanocrystalline films exhibit larger amount of stacking faults. ► Nanostructuring does not worsen the corrosion resistance in chloride medium.

0257-8972/$ – see front matter © 2011 Published by Elsevier B.V.
doi:10.1016/j.surfcoat.2011.05.047

Surface & Coatings Technology xxx (2011) xxx–xxx

Contents lists available at ScienceDirect

Surface & Coatings Technology

journal homepage: www.elsevier.com/locate/surfcoat

A comparison between fine-grained and nanocrystalline electrodeposited Cu–Ni films. Insights on mechanical and corrosion performance

E. Pellicer [a,*], A. Varea [a], S. Pané [b], K.M. Sivaraman [b], B.J. Nelson [b], S. Suriñach [a], M.D. Baró [a], J. Sort [c]

[a] Departament de Física, Facultat de Ciències, Universitat Autònoma de Barcelona, E-08193 Bellaterra, Spain
[b] Institute of Robotics and Intelligent Systems (IRIS), ETH Zurich, CH-8092 Zurich, Switzerland
[c] Institució Catalana de Recerca i Estudis Avançats (ICREA) and Departament de Física, Universitat Autònoma de Barcelona, E-08193 Bellaterra, Spain

ARTICLE INFO

Article history:
Received 17 September 2010
Accepted in revised form 23 May 2011
Available online xxxx

Keywords:
Nanocrystalline films
Copper–nickel alloy
Electrodeposition
Mechanical properties
Corrosion

ABSTRACT

$Cu_{1-x}Ni_x$ ($0.43 \leq x \leq 1.0$) films were electrodeposited from citrate–sulphate baths at different current densities onto Cu/Ti/Si (100) substrates with the addition of saccharine as a grain-refining agent. The Cu–Ni alloy films produced from saccharine-free baths were fine-grained (crystallite size of ~400 nm). The addition of saccharine to the electrolytic solution induced a dramatic decrease in crystal size (down to ~27 nm) along with a reduction in surface roughness. Although the effect of saccharine on pure Ni films was less obvious, significant changes were observed due to the presence of saccharine in the bath during the alloying of Cu with Ni. Compared to fine-grained Cu–Ni films, the nanocrystalline films exhibited lower microstrains and a larger amount of stacking faults as observed by X-ray diffraction. These features enhance the mechanical properties of the Cu–Ni alloys, making the nanocrystalline Cu–Ni films superior to both the corresponding fine-grained films and pure Ni films. In particular, hardness in fine-grained films varied from 4.2 ($x = 0.43$) to 5.4 GPa ($x = 0.86$), whereas hardness varied between 6.7 and 8.2 GPa for nanocrystalline films of similar composition. In addition, wear resistance and elastic recovery were enhanced. Nanostructuring did not significantly affect corrosion resistance of Cu–Ni alloys in chloride media. Although the corrosion potential shifted slightly towards more negative values, the corrosion current density decreased, thereby making the electrodeposition nanostructuring process an effective tool to improve the overall properties of the Cu–Ni system.

1. Introduction

Nanostructured materials benefit from improved, and sometimes novel, physical and chemical properties compared to conventional coarse-grained materials, thus creating opportunities for advanced technological applications. Amongst the material properties of metals that can be enhanced by nanostructuring, mechanical properties currently receive considerable attention from both fundamental and applied perspectives [1–3]. Of the investigations that exist, the focus is either on understanding the mechanical behaviour of nanostructured materials from a fundamental perspective, or exploiting the new properties that result from nanostructuring. Compared to conventional coarse-grained materials, nanocrystalline metals with grain sizes typically smaller than 100 nm possess lower elastic moduli, higher tensile strength and hardness, increased ductility and fatigue resistance, and, under certain conditions, superplastic behaviour [4–7]. Some of these characteristics were theoretically predicted by Gleiter et al. two decades ago [8] and have since then been experimentally verified by a number of researchers. In addition, the measurement of the mechanical properties of nanostructured metallic materials greatly depends on the kind of sample considered, i.e. thin films, thick films or bulk specimens. Compared with nanostructured bulk materials, the assessment of the mechanical properties of nanocrystalline metallic thin films still remains a rather unexplored field [9].

Electrodeposition is one of the best techniques to prepare nanocrystalline metallic thin films with thicknesses ranging from hundreds of nanometers to tens of micrometres. This is an old yet versatile technique with several attributes that make it extremely well suited for micro- and nanotechnologies. The process can be scaled up or down, deposition can be performed on a wide variety of substrates, it can be performed near room temperature from water-based, environmentally friendly electrolytes, and it is able to produce pore-free coatings at high rates. With the advent of nanotechnology, electrodeposition has gained many supporters within the scientific community largely because it is a simple, cost-effective technique and less time-consuming compared to physical methods such as sputtering or evaporation. Furthermore, physical methods are generally limited to thinner films (up to 1–2 μm), a restriction that can be a drawback for some micro- and nano-electromechanical systems where thicker films are desired. Due to these reasons, the development of electroplated films either by direct or pulse methods to

Q1 * Corresponding author. Tel.: +34 935811401; fax: +34 935812155.
E-mail address: Eva.Pellicer.icn@uab.cat (E. Pellicer).

0257-8972/$ – see front matter © 2011 Published by Elsevier B.V.
doi:10.1016/j.surfcoat.2011.05.047

produce nanocrystalline sheets of metals (such us Co, Ni and Cu) [10–12] and metallic alloys (e.g. Co–Pt, Co–Ni, Ni–W, Co–Fe–Ni) [13–16] is of increasing interest.

The first investigations of the electrodeposition of nickel films with fine grain sizes used saccharine and coumarin as additives [17]. Since then, considerable effort has been directed towards the development of nanocrystalline nickel films plated in either re-formulated traditional or newly formulated baths [18–22]. The Watts bath, with or without organic additives, remains the most commonly employed [23–26]. To the basic Watts bath (nickel sulphate, nickel chloride and boric acid) saccharine is typically added as a grain refining and stress relieving agent. In fact, saccharine performs these functions well for many metals and alloys deposited from a variety of baths [27–29]. Despite the numerous studies performed regarding the various strategies towards grain refinement, reported data is, in some cases, inconsistent across different investigations. It is, therefore, difficult to draw conclusions, especially when comparing the mechanical properties for a given metal in its nanocrystalline, fine- or coarse-grained forms. This lack of systemisation becomes even more evident when dealing with alloys, for which the literature is limited. This problem arises in part from the difficulty of explaining the extent to which various factors, both the ones inherent in the system considered (e.g. solution hardening effects, stacking fault energies of each metal), and the electrodeposition conditions (e.g. bath formulation, applied current density, bath temperature) contribute to the obtained properties. This work is aimed at providing a more comprehensive framework by a clear comparison between fine-grained and nanocrystalline Cu–Ni thin films. The Cu–Ni system has been chosen for several reasons; it can be electroplated from aqueous electrolytes [30,31], it shows total miscibility over the complete composition range, its production is much less expensive compared to Co-based alloys or alloys containing metals like W and Mo. Moreover, the Cu–Ni alloys exhibit interesting functional properties such us good corrosion resistance in marine environments, anti-biofouling properties, and, depending on their composition, either paramagnetic or ferromagnetic behaviour [32–34]. Nanostructuring has been reported to have either beneficial or detrimental effects on the corrosion performance of metallic materials depending on the system under study. Though the corrosion behaviour of bulk Cu–Ni alloys in several environments is well documented [35–38], the effects induced by nanostructuring on the corrosion resistance of electroplated Cu–Ni films still remains poorly understood.

In this study, Cu_{1-x}–Ni_x ($0.43 \le x \le 1.0$) films were electroplated from a sulphate-based bath containing citrate as a complexing agent, both with and without the addition of saccharine. The purpose of the present investigation is two-fold; the assessment of the effects of alloying copper with nickel, and a direct comparison between the properties of fine-grained and nanocrystalline Cu_{1-x}–Ni_x films with similar composition. The hardness, Young's modulus and wear characteristics of the films were evaluated by depth-sensing nanoindentation which is a particularly well-suited technique for coatings [39]. Apart from the mechanical properties, the morphology, microstructure, surface roughness and corrosion performance of these films were studied in detail and key relationships between these properties outlined.

2. Experimental procedure

The metallic films were obtained by direct current electrodeposition in a one-compartment thermostatised three-electrode cell using a PGSTAT30 Autolab potentiostat/galvanostat (Ecochemie). Cu–Ni alloy films were deposited from an electrolyte containing 184 g/L $NiSO_4 \cdot 6H_2O$, 6.24 g/L $CuSO_4 \cdot 5H_2O$, 87 g/L $Na_3C_6H_5O_7 \cdot 2H_2O$, 0.2 g/L $NaC_{12}H_{25}SO_4$ (*saccharine-free bath, SFB*) and 0.5 g/L $C_7H_5NO_3S$ (*saccharine-containing bath*, *SCB*). Nickel films were obtained from an electrolyte containing 190 g/L $NiSO_4 \cdot 6H_2O$, 87 g/L $Na_3C_6H_5O_7 \cdot 2H_2O$, 0.2 g/L $NaC_{12}H_{25}SO_4$ (*saccharine free-bath, SFBN*) and 0.5 g/L $C_7H_5NO_3S$ (*saccharine-containing bath, SCBN*). The electrolyte volume was 100 ml. Analytical grade reagents and ultrapure water (18 MΩ cm) were used to prepare the electrolyte. For all solutions, the pH was fixed at 4.5 and the temperature at 30 °C. Silicon (100) substrates with e-beam evaporated Ti (100 nm)/Cu (500 nm) adhesion/seed layers were used as working electrodes (WE), which were positioned vertically within the electrolyte. The working area was 6×5 mm^2. A double junction Ag|AgCl (E = +0.210 V/SHE) reference electrode (Metrohm AG) was used with 3 M potassium chloride (KCl) inner solution and an interchangeable outer solution. The outer solution was made of 1 M sodium sulphate. A platinum spiral served as counter electrode. Prior to deposition, the copper surface was first degreased with acetone followed by isopropyl alcohol and water and, finally, dipped in diluted sulphuric acid to remove any oxides and organic residues present on the copper surface. The backside of the silicon substrate was insulated by painting it with a nonconductive lacquer to ensure that only the copper surface was conductive. Before each experiment, the electrolyte was de-aerated with nitrogen gas for 10 min through a glass purge pipe which provided a vigorous stream of nitrogen. A blanket of nitrogen was maintained on top of the solution during the deposition. Deposition was conducted galvanostatically under mild stirring (200 rpm) using a magnetic stirrer bar. The electrical charge was adjusted across all depositions to attain similar film thicknesses. After deposition, the films were thoroughly rinsed in water and stored in air.

The chemical composition of the films was determined by energy dispersive X-ray spectroscopy (EDXS). Metal proportions are expressed in atomic percentage (at.%). The morphology was examined by scanning electron microscopy (SEM) on a JEOL JSM-6300 microscope. The average film thickness was determined from four-point measurements over the entire surface by interferometric profilometry. The structure of the deposits was studied by X-ray diffraction (XRD) and transmission electron microscopy (TEM). X-ray diffraction patterns were recorded on a Philips X'Pert diffractometer using the Cu Kα radiation in the 38°–110° 2θ range (0.03° step size, 10 s holding time). The global structural parameters, such as crystallite sizes, $<D>$ (defined here as the average coherently diffracting domain sizes), and microstrains or atomic level deformations, $<\varepsilon^2>^{1/2}$, were evaluated by fitting the full XRD patterns using the Materials Analysis Using Diffraction (MAUD) Rietveld refinement programme [40–42]. This software includes a formalism to quantitatively evaluate the stacking fault probability, α_{SF} [41,43]. TEM characterisation was carried out on a JEOL JEM-2011 microscope operated at 200 kV. For the planar-view observations, the films were thinned by ion milling, which was performed on both sides of the film in order to remove any surface contamination. Roughness of the films was characterised by atomic force microscopy (AFM) using a Dual Scope™ C-26 system (Danish Micro Engineering) working in AC mode. A commercial silicon tip (50–100 KHz resonance frequency) was used to scan surface areas of 5×5 μm^2. Both the peak-to-valley distance and the root-mean-square (RMS) deviation values were extracted from the images.

The mechanical properties (hardness and reduced elastic modulus) were evaluated by nanoindentation operating in the load control mode using a UMIS device from Fischer–Cripps Laboratories equipped with a Berkovich pyramid-shaped diamond tip. The value of maximum applied force was chosen to be 10 mN to ensure that the maximum penetration depth during the tests was kept below one tenth of the overall film thickness. This is considered a necessary condition to avoid substrate influence on measured mechanical properties [44]. The thermal drift during nanoindentation was kept below 0.05 nm/s. Corrections for the contact area (calibrated with a fused quartz specimen), instrument compliance, and initial penetration depth were applied. For nanoindentation testing the mechanical properties of the film can be extracted from the load–unload curve

Please cite this article as: E. Pellicer, et al., Surf. Coat. Technol. (2011), doi:10.1016/j.surfcoat.2011.05.047

making direct measurements on the indentations unnecessary. The hardness (H) and reduced elastic modulus (E_r) values were derived from the load–displacement curves at the beginning of the unloading segment using the method of Oliver and Pharr [45]. From the initial unloading slope the contact stiffness, S, was determined as:

$$S = \frac{dP}{dh} \tag{1}$$

where P and h denote the applied load and penetration depth during nanoindentation, respectively. The elastic modulus was evaluated based on its relationship with the contact area, A, and contact stiffness:

$$S = \beta \frac{2}{\sqrt{\pi}} E_r \sqrt{A} \tag{2}$$

Here, β is a constant that depends on the geometry of the indenter ($\beta = 1.034$ for a Berkovich indenter) [44], and E_r is the reduced Young's modulus, defined as:

$$\frac{1}{E_r} = \frac{1-\nu^2}{E} + \frac{1-\nu_i^2}{E_i} \tag{3}$$

The reduced modulus takes into account the elastic displacements that occur in both the specimen, with Young's modulus E and Poisson's ratio ν, and the diamond indenter, with elastic constant E_i and Poisson's ratio ν_i. For diamond, $E_i = 1140$ GPa and $\nu_i = 0.07$. Hardness (H) was calculated from:

$$H = \frac{P_{Max}}{A} \tag{4}$$

where P_{Max} is the maximum load applied during nanoindentation. Finally, the elastic recovery was evaluated as the ratio between the elastic (W_{el}) and the total (plastic + elastic) (W_{tot}) energies during nanoindentation. These energies were calculated from the nanoindentation experiments as the areas between the unloading curve and the x-axis (W_{el}) and between the loading curve and x-axis (W_{tot}) [44]. The results presented here represent the statistical average of a set of 100 indentations for each sample.

The corrosion performance of the films was evaluated by electrochemical techniques in a conventional three-electrode cell. Corrosion tests were conducted in aerated 3.5 wt.% NaCl solution under quiescent conditions at room temperature. The outer solution of the Ag|AgCl reference electrode was made of 1 mol dm^{-3} NaCl. A platinum spiral served as a counter electrode. After sample immersion in the 3.5 wt.% NaCl solution, the steady state potential (E_{ss}) was measured until fluctuations less than 10 mV h^{-1} were observed. This process was usually complete within 3 to 4 h. The electrochemical polarisation was scanned from the steady-state potential to E_{ss} − 300 mV cathodically and then to E_{ss} + 300 mV anodically with a scan rate of 0.1 mV s^{-1}. The reproducibility of the data related to the corrosion potential (E_{corr}) and the corrosion current density (j_{corr}) was monitored using four samples per film (0.3 cm^2 exposed area), and average results are reported.

3. Results and discussion

3.1. Electrochemical preparation of the thin films

Fig. 1 shows the E-t transients for Cu–Ni plated onto Cu/Ti/Si (100) substrates from saccharine-free and saccharine-containing baths at two different applied current densities, −10 and −40 mA cm^{-2}. For a given applied current density, the stabilised potential (E_S) slightly shifts towards more negative values with the addition of saccharine to the bath. The same trend was observed when recording cathodic linear sweep curves (not shown), both for Ni and Cu–Ni systems. Since saccharine molecules adsorb onto the electrode and interfere with the normal metal deposition by blocking the attachment of ad-atoms, the cathodic overpotential increases [46,47]. In fact, the double layer capacitance is expected to decrease as a consequence of the blocking adsorption of saccharine. Also, the addition of saccharine changes the composition of the Helmholtz electrochemical double layer, thus variations in cathode polarisation are expected [48]. This shift is more pronounced at higher current densities, suggesting that, as observed for other metals and alloys, the inhibiting effect on ion discharge is enhanced.

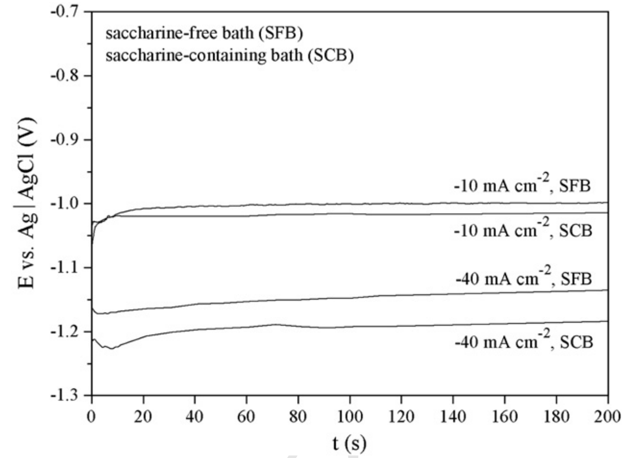

Fig. 1. E-t transients for Cu–Ni deposition onto Cu/Ti/Si (100) substrates at the indicated current densities.

3.2. Morphological and compositional characterisation

The morphology of the Cu–Ni films obtained galvanostatically from the SFB and SCB baths is shown in Fig. 2a–d. Charge density was tuned to obtain a film thickness of 3.0 ± 0.2 μm. Optimisation was possible by combining Faraday's law with the current efficiency, which depends on both the bath composition and the applied current density. The deposits obtained from the SFB at −10 mA cm^{-2} displayed edged grains featuring cauliflower-like clusters in some regions (Fig. 2a). At a higher current density, the grains became rounded and their size distribution narrowed (Fig. 2c). Conversely, the SCB bath yielded smooth and almost featureless deposits irrespective of the applied current density (Fig. 2b and d), indicating a decrease in surface roughness. In all cases, deposits were crack-free and pitting was not observed, probably due to the anti-pitting effect brought by the sodium lauryl sulphate wetting agent [49].

Pure nickel deposits of a similar thickness were also prepared from a bath in which copper sulphate was replaced by nickel sulphate in order to maintain the same ionic strength. The morphology of the films, produced from either the saccharine-free bath (SFBN) or saccharine-containing bath (SCBN) at −40 mA cm^{-2}, was different from the films previously described. Unlike the Cu–Ni films, deposits obtained from the SFBN showed less rounded clustered grains (cf. Fig. 2c and e). Most importantly, the morphology of the nickel deposits plated from the SCBN could be resolved, giving a cotton-like appearance (cf. Fig. 2d and f). It is, therefore, clear that copper has some influence on the deposition of Ni which is observed in the deposit morphology.

Please cite this article as: E. Pellicer, et al., Surf. Coat. Technol. (2011), doi:10.1016/j.surfcoat.2011.05.047

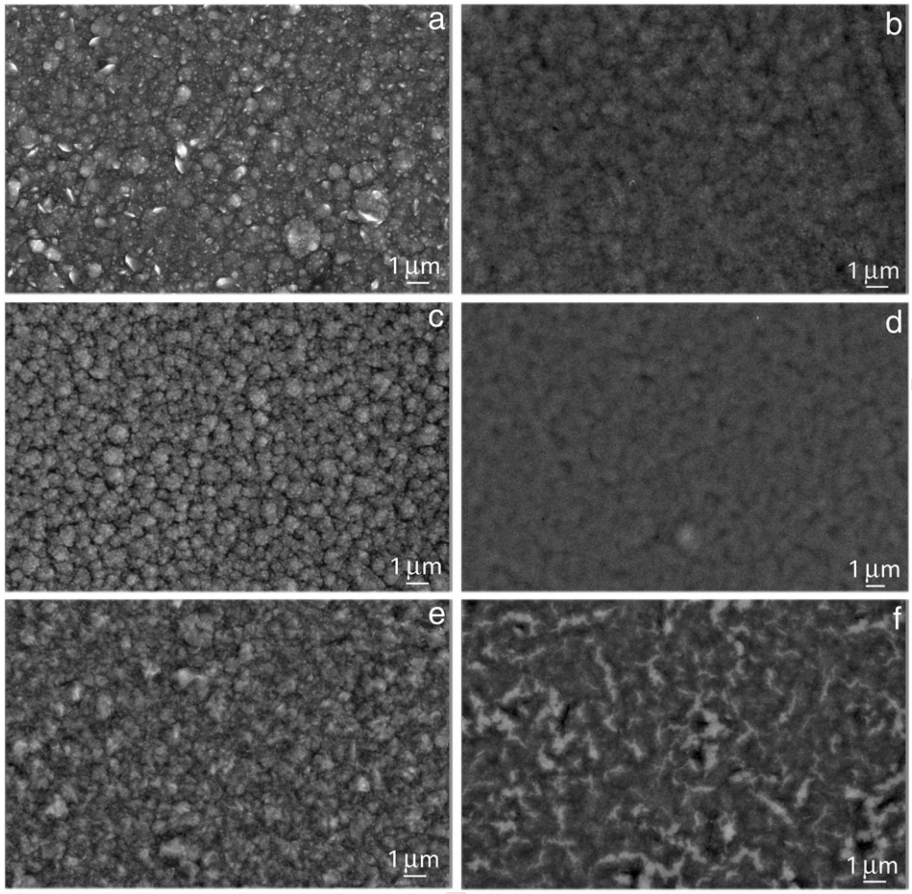

Fig. 2. SEM images of Cu–Ni films deposited at $j = -10$ mA cm^{-2} from (a) saccharine-free bath (SFB) with 43 at.% Ni and (b) saccharine-containing bath (SCB) with 45 at.% Ni, and deposited at $j = -40$ mA cm^{-2} from (c) SFB with 86 at.% Ni and (d) SCB with 87 at.% Ni. SEM images of Ni films deposited at $j = -40$ mA cm^{-2} from (e) saccharine-free bath (SFBN) and (f) saccharine-containing bath (SCBN).

EDX analyses on the Cu–Ni films revealed that nickel content increased with current density. In the presence of citrate as a complexing agent, copper is typically discharged under mass-transport control, whereas nickel remains under activation control within a wide potential range [50,51]. Therefore, an increase in the overvoltage promotes nickel discharge and, ultimately, leads to deposits with higher nickel contents. At a given current density the composition remained nearly identical regardless of the presence of saccharine in the bath. Only a slight enrichment in Ni (at around 1–2 at.%) was detected in the films obtained from the SCB, probably due to the greater overpotential. At $j = -10$ mA cm^{-2} the Ni content was 43–45 at.% and increased to 86–87 at.% at $j = -40$ mA cm^{-2}.

Although the smoothing effect induced by saccharine on the topography was visually apparent, quantitative measurements of surface roughness were carried out by AFM. Typical 2D topographical images of the Cu–Ni films obtained from the SFB and SCB are shown in Fig. 3. The former featured rough surfaces with edged grains, whilst the latter displayed a surface with lower roughness. The root-mean-square deviation (RMS) and the peak-to-valley distance values for 5×5 µm^2 scanned areas are listed in Table 1. The AFM analyses corroborated visual observations, i.e. a loss of metallic lustre and, therefore, higher surface roughness (and larger peak-to-valley distances) in the Cu–Ni films prepared from the SFB compared to the SCB derived ones. Although smoother deposits were produced by increasing the current density in the SFB, a drastic reduction of surface roughness was accomplished with the addition of saccharine to the bath [52]. Roughness decrease was less effective, yet noticeable, for pure Ni films.

3.3. Structural characterisation

The structural properties of the thin films were studied by XRD and TEM analyses. All films showed a face-centred cubic (fcc) structure, but the width of the fcc reflections greatly varied across the different samples. The XRD measurements confirmed the formation of Cu–Ni solid solution in all samples. The role of citrate is to reduce the large difference in the standard reduction potentials of copper (+0.34 V) and nickel (−0.25 V), thus allowing their co-deposition [31]. Fig. 4 shows a detail of the (111) and (200) fcc reflections for Cu–Ni and pure Ni films. The narrow peaks located at around $2\theta = 43.3°$ and 50.5° belong to the Cu seed-layer, which also displayed an fcc structure. As the alloy became enriched in Ni, a shift in the Cu–Ni peak positions towards higher angles was observed (see Fig. 4a and b). For a given composition, the Cu–Ni films obtained from the SCB featured much broader reflections, indicating smaller grain sizes in agreement with previous morphological observations. The peaks were not precisely centred at the same 2θ, but at slightly higher angles corresponding to a richer Ni composition. Notice that the stabilised potential (E_S) of the galvanostatic curves shifted towards more negative values due to saccharine addition, thus favouring Ni discharge. The Ni films plated from the SCBN also displayed wider reflections (Fig. 4c). On the other hand, the difference in the width of the (111) and (200) peaks for all samples is indicative of the existence of stacking faults. To rationalise all these trends from quantitative structural factors, the full XRD patterns were Rietveld-refined. The extracted cell parameters, crystallite sizes, microstrains and stacking fault probabilities are listed in Table 2. As an example, Fig. 4d shows

Please cite this article as: E. Pellicer, et al., Surf. Coat. Technol. (2011), doi:10.1016/j.surfcoat.2011.05.047

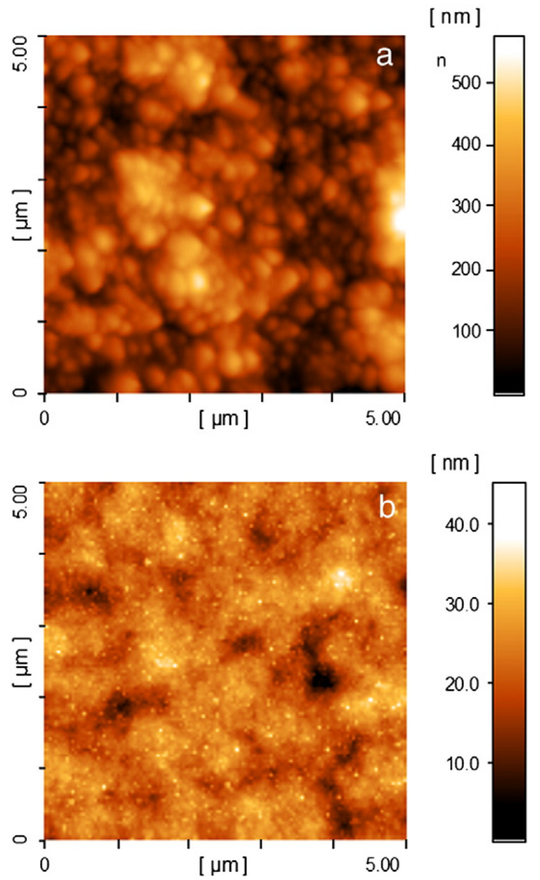

Fig. 3. AFM topographical images of (a) $Cu_{0.57}Ni_{0.43}$ film obtained from the SFB and (b) $Cu_{0.55}Ni_{0.45}$ film obtained from the SCB. Note that the scale bar on the right side of the images indicates distance along the z-axis (i.e. depth).

the Rietveld fitting of the XRD pattern corresponding to the nanocrystalline $Cu_{0.13}Ni_{0.87}$ film in the 42–55° 2θ region.

The main trends regarding crystallite size (*i*), microstrains (*ii*) and stacking fault probabilities (*iii*) are summarised below:

(i) All samples plated from saccharine-free baths (SFB/SFBN) had crystallite sizes at approximately 400 nm, i.e. fine-grained. An increase of the current density made the crystallise size of the Cu–Ni alloy decrease slightly, as expected due to the higher deposition rate. The addition of saccharine to the plating solution induced a dramatic crystallite size reduction yielding nanocrystalline films. TEM images further corroborated these results (Fig. 5). Moreover, the crystallite size remained nearly the same (26–29 nm) irrespective of the applied current density, which suggests that its value is mainly controlled by the saccharine additive in SCB. In contrast, though the crystallite size of pure Ni films also decreased with the addition of saccharine to the bath, it remained within the fine-grained regime. We denote the Ni films plated from the SFBN by *fine-grained nickel* and the ones plated from SCBN by *ultrafine-grained nickel*. Notice that when saccharine was absent from the bath, the alloying of Cu with Ni did not change the structure apart from the expected increase in the cell parameter (compare the fine-grained Ni with the $Cu_{0.14}Ni_{0.86}$ films in Table 2). TEM images were in accordance with these findings (see Fig. 5a and b). Conversely, when saccharine was present in the electrolyte, alloying Cu with Ni did make a difference; the crystal size reduced by an order of magnitude, from 207 to 29 nm with just 13 at.% of Cu being dissolved in the Ni lattice (compare the ultrafine-grained Ni with the nanocrystalline $Cu_{0.13}Ni_{0.87}$ films in Table 2, and TEM images of Fig. 5a and c).

(ii) Saccharine is also responsible for the decrease in microstrain. Strain is common in electrodeposits [53]. Macrostrain develops over large areas, arises from either tensile or compressive stresses, and leads to XRD peak shifting. Microstrains (non-uniform strains) develop over small distances and are a distribution of d-spacings thus leading to XRD peak broadening. The values reported in Table 2 refer to this class of strains. Saccharine is known to be an excellent tensile macrostress reducing agent. Recently, it has been reported that the coalescence of Ni grains in films electroplated from saccharine-free sulfamate baths is a tensile stress controlled process, whilst films with compressive stress or low tensile stress are obtained in the presence of saccharine [54]. In fact, the Ni films prepared from the SFBN were prone to peeling from the copper surface, mostly due to high tensile stress. The addition of saccharine to the bath led to properly adhering deposits owing to the compressive effect conferred by saccharine.

(iii) From Table 2, it is clear that the number of planar defects increases when the Cu–Ni alloy is nanocrystalline. The same is true for pure Ni films, i.e. the finer the grain size, the higher the stacking fault probability. This is in agreement with the large number of intragranular nanotwins detected by High Resolution TEM in the SCB plated films (Fig. 5d). From a thermodynamic viewpoint, the formation of twins decreases the total interfacial energy [55]. Because twins preferably nucleate at grain boundaries or triple junctions, one might expect that the stacking fault probability should be higher for larger amounts of grain boundaries (i.e. nanocrystalline films). However, the increased probability of twinning does not arise solely from the larger number of grain boundaries. The role of saccharine as an adsorbate creates physicochemical considerations that must also be taken into account. It has been reported for Ni electrodeposits that the presence of surface-active substances in the electrolytic solution clearly has an effect on stacking fault dislocations and twins [56]. In the late 70s it was suggested that saccharine increases the probability of twinning in Ni electrodeposits because of its preferential adsorption onto (111) planes, which results in an increased amount of crystal mass in twin orientation [57]. The same authors demonstrated that the probability of twinning is additive-dependent (for example, the butyne-2-diol, a typical brightener used in the plating industry, was reported to be inactive with respect to the formation of twin stacking faults). The addition of additives is not strictly necessary to generate nanotwins; an increase of current density is sufficient to enhance their formation. It is known that growth twins are frequently formed when electrodepositing metals with appropriate stacking fault energies [1]. In particular, twins are easily formed in fcc metals with low stacking fault energies, as is the case with Cu and Ni [58]. Moreover, faster deposition rates will, in principle, lead to higher twin densities since both metals have relatively large twin boundary energies [1]. Whilst the mechanism of twin

Table 1
RMS and peak-to-valley distance values extracted from topographical AFM images of Cu–Ni and Ni films.

Bath[a]	$-j$ (mA cm^{-2})	Film	RMS (nm)	Peak-to-valley (nm)
SFB	10	$Cu_{0.57}Ni_{0.43}$	43	266
SCB	10	$Cu_{0.55}Ni_{0.45}$	5	36
SFB	40	$Cu_{0.14}Ni_{0.86}$	20	127
SCB	40	$Cu_{0.13}Ni_{0.87}$	4	30
SFBN	40	Ni	21	128
SCBN	40	Ni	17	111

[a] SFB: saccharine-free Cu–Ni bath, SCB: saccharine-containing bath, SFBN: saccharine-free Ni bath, SCBN: saccharine-containing Ni bath.

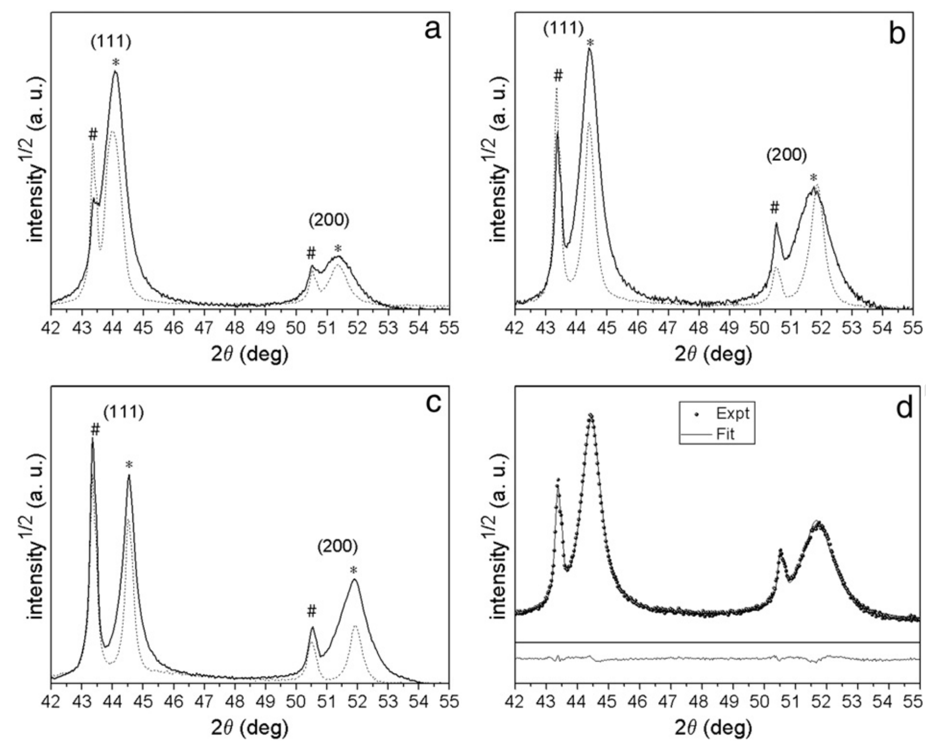

Fig. 4. Detail of the (111) and (200) X-ray reflections for (a) Cu rich Cu–Ni, (b) Ni-rich Cu–Ni and (c) pure Ni films obtained from saccharine-containing (solid line) and saccharine-free (dotted line) baths. Peaks denoted by # and * belong to the Cu-seed layer and the electroplated film, respectively. d) Rietveld fitting of one of the spectra shown in (b) (nanocrystalline $Cu_{0.13}Ni_{0.87}$ film) and the corresponding difference between the experimental and the calculated profiles.

formation in metal electroplating is not fully understood, it is generally accepted that it is a kinetically driven process in such a way that nucleation and growth rate of twins are controlled by the deposition conditions. Lu et al. have experimentally verified that nanotwining in electroplated Cu increases with deposition rate (i.e. with an increase of the applied current density) [55].

3.4. Mechanical properties

Fig. 6 shows representative load-unload indentation curves of the electrodeposited films. For each composition, the penetration depth attained at the end of the unloading segment is lower for the film having smaller crystallite sizes. This indicates that the nanocrystalline Cu–Ni thin films are mechanically harder than the corresponding fine-grained films. For the Ni samples, grain refinement also accounts for the lower penetration depth observed in the SCBN plated films, again indicating enhanced hardness. Table 3 lists the hardness (H), reduced Young's modulus (E_r) together with H/E_r, H^3/E_r^2 and W_{el}/W_{tot} ratios for all films extracted from the corresponding indentation curves (where W_{el} and W_{tot} denote the elastic and total indentation energies, respectively).

The increase of the Ni content in the alloy increased hardness both within the fine-grained (from 4.2 to 5.4 GPa) and nanocrystalline (from 6.7 to 8.2 GPa) domains, as expected due to solid solution hardening [59]. Amongst the samples tested, the nanocrystalline $Cu_{0.13}Ni_{0.87}$ film was the hardest ($H = 8.2$ GPa), even harder than the two pure Ni samples. From the point of view of chemical composition alone, it would be expected that pure Ni would be mechanically harder than the Cu–Ni alloy since Cu is softer than Ni. However, the strength of a solid (i.e., its resistance against plastic deformation) is not only sensitive to the solid's chemical composition but also to its microstructure. In particular, larger hardness is expected for smaller crystallite sizes. Nanostructured metals have a larger density of grain boundaries than fine-grained or coarse-grained metals. Grain boundaries are efficient in disrupting the propagation of dislocations through a material. The enhanced hardness arising from the reduced crystallite sizes is explained by the Hall–Petch relationship [6]. In addition, the presence of intragranular nanotwins contributes to material strength, since twin boundaries are able to block the propagation of slip bands [55]. Coherent twin boundaries behave in a similar manner to grain boundaries by acting as obstacles to strain propagation.

E_r exhibited the same trend as H with regard to composition. Since the elastic modulus of Ni is higher than for Cu, E_r increased with the Ni content. For a given composition, E_r was slightly lower for the film with smaller crystallite sizes except for the Cu-rich Cu–Ni samples. Taking the Poisson's ratio for nickel ($\nu_i = 0.31$) [60] into account, the

Table 2
Global structural parameters obtained after Rietveld refinement of the full XRD patterns of $Cu_{1-x}Ni_x$ and Ni films.

Bath[a]	Film	Lattice cell parameter a ($\pm 10^{-3}$ Å)	Crystallite size <D> (± 3 nm)	Microstrain $<\varepsilon^2>^{1/2}$ ($\pm 10^{-5}$)	Stacking fault probability α_{SF} ($\pm 5 \times 10^{-4}$)
SFB	$Cu_{0.57}Ni_{0.43}$	3.561	413	$3 \cdot 10^{-3}$	0.001
SCB	$Cu_{0.55}Ni_{0.45}$		26	$2 \cdot 10^{-4}$	0.007
SFB	$Cu_{0.14}Ni_{0.86}$	3.532	379	$8 \cdot 10^{-4}$	0.004
SCB	$Cu_{0.13}Ni_{0.87}$		29	$2 \cdot 10^{-4}$	0.007
SFBN	Ni	3.523	387	$3 \cdot 10^{-4}$	0.002
SCBN	Ni		207	$2 \cdot 10^{-5}$	0.008

[a] SFB: saccharine-free Cu–Ni bath, SCB: saccharine-containing bath, SFBN: saccharine-free Ni bath, SCBN: saccharine-containing Ni bath.

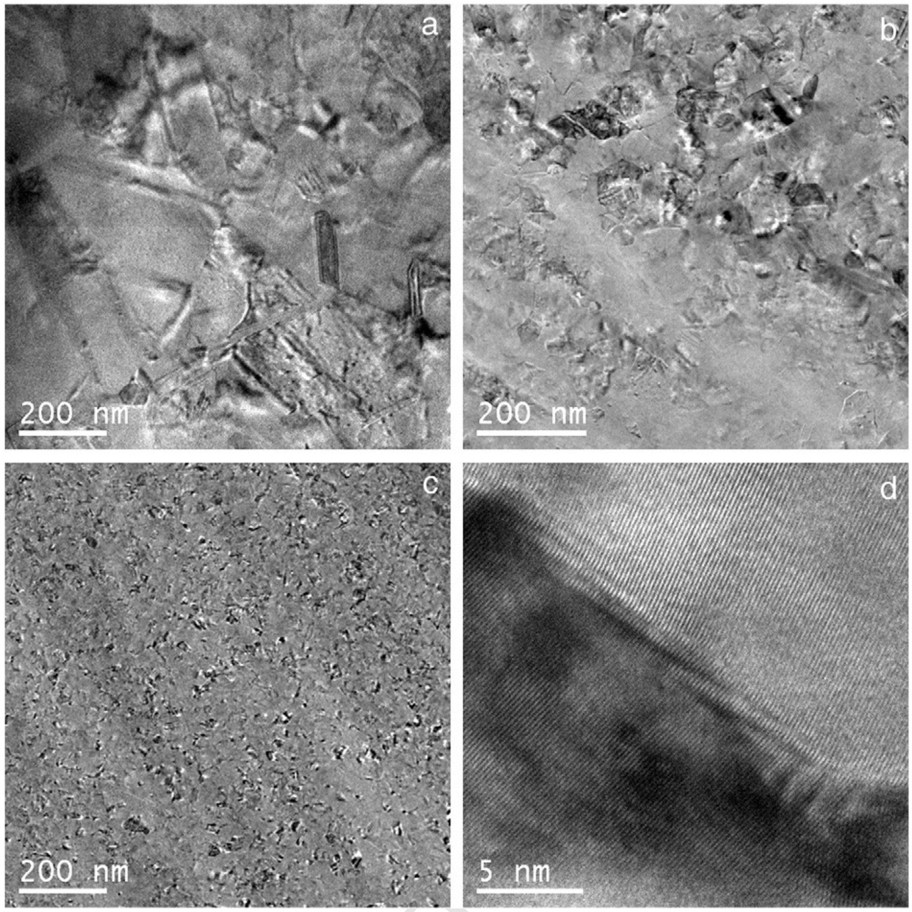

Fig. 5. TEM images of (a) ultrafine-grained Ni, (b) fine-grained $Cu_{0.14}Ni_{0.86}$, and (c) nanocrystalline $Cu_{0.13}Ni_{0.87}$ films. (d) HRTEM image of a twinned region of the sample shown in (c).

Young's modulus is 214 and 210 GPa for fine-grained and ultrafine-grained nickel films, respectively. Similarly, if one assumes the Poisson's ratio of Cu–Ni alloy to be $\nu_i = 0.34$ [61], the Young's modulus varies from 170 to 208 GPa within the fine-grained regime, and from 179 to 204 GPa within the nanocrystalline regime. The Young's modulus of nanocrystalline materials is usually lower than in coarse-grained materials by as much as 70% in some cases [62–64], due to the occurrence of porosity or the increased interatomic spacings in interface regions [62,65]. Regardless, our variations in the elastic modulus are rather small, probably because electrodeposition is known to produce pore-free coatings, which explains why similar E_r values were obtained for fine-grained and nanocrystalline Cu–Ni films. Our findings are in agreement with other works in which the reduction in the Young's modulus value was found to be less pronounced than expected. For instance, Legros et al. did not find any change in the Young's modulus in Ni and Cu films with grain sizes approaching 25 nm when evaluated by microsample tensile testing [66].

The hardness to elastic modulus ratio, H/E (or H/E_r if the reduced Young's modulus is used) is recognised to provide an indirect, yet reliable, assessment of the wear behaviour of a material [67]. Notice that the H/E_r ratio for the nanocrystalline Cu–Ni (and ultrafine-grained Ni) films was higher than in fine-grained ones, indicating that the former displays enhanced wear resistance. The same factors account for the H^3/E_r^2 ratio, which is a good indicator of the resistance to plastic deformation [68,69]. The higher this index, the higher the energy absorbed by the material before fracture. Significantly, the nanocrystalline $Cu_{0.13}Ni_{0.87}$ film displayed higher H/E_r and H^3/E_r^2 ratios than the ultrafine-grained Ni sample. The singular microstructural attributes of nanocrystalline Ni-rich $Cu_{1-x}Ni_x$ films can again be used to explain this result. Finally, we evaluated the elastic recovery, expressed as W_{el}/W_{tot} in percentage, to gain information about the deformation degree recovered during unloading. The W_{el}/W_{tot} ratio correlated well with both H/E_r and H^3/E_r^2 (elastic recovery is closely related to H/E) [68]. Whilst W_{el}/W_{tot} increased with Ni content, smaller crystallite sizes also led to higher W_{el}/W_{tot} [70].

3.5. Corrosion behaviour

The corrosion performance of the films was evaluated in aerated 3.5 wt.% NaCl. Because Cu–Ni alloys are commonly used in applications involving sea-water, a chloride-containing medium was chosen as a test solution. Typical potentiodynamic polarisation curves are shown in Fig. 7. While the cathodic branches did not reveal any special feature, the anodic branch displayed an oxidation peak followed by a passive region in some cases (see the grey curve). The oxidation peak is likely to be attributed to the formation of a passive oxide film that further protects the material. The presence of oxides as the primary corrosion products was identified in bulk Cu–Ni alloys exposed to chloride media [35,36]. Pure Ni films did not show an active–passive transition, but rather a monotonous increase in the anodic current. The E_{corr} and j_{corr} values were calculated using the Tafel extrapolation method and are listed in Table 4. Due to peeling of the fine-grained Ni films, only the results for ultrafine-grained Ni are reported. On comparing the behaviour of ultrafine-grained Ni with fine-grained $Cu_{0.14}Ni_{0.86}$ film, it can be seen that E_{corr} is nearly the same but j_{corr} decreases. Thus, the alloying of Cu with Ni clearly has a beneficial effect on corrosion performance, especially bearing in mind that the average crystallite size in the $Cu_{0.14}Ni_{0.86}$ film is higher than in ultrafine-grained nickel (379 nm vs. 207 nm). Rajasekaran and

Please cite this article as: E. Pellicer, et al., Surf. Coat. Technol. (2011), doi:10.1016/j.surfcoat.2011.05.047

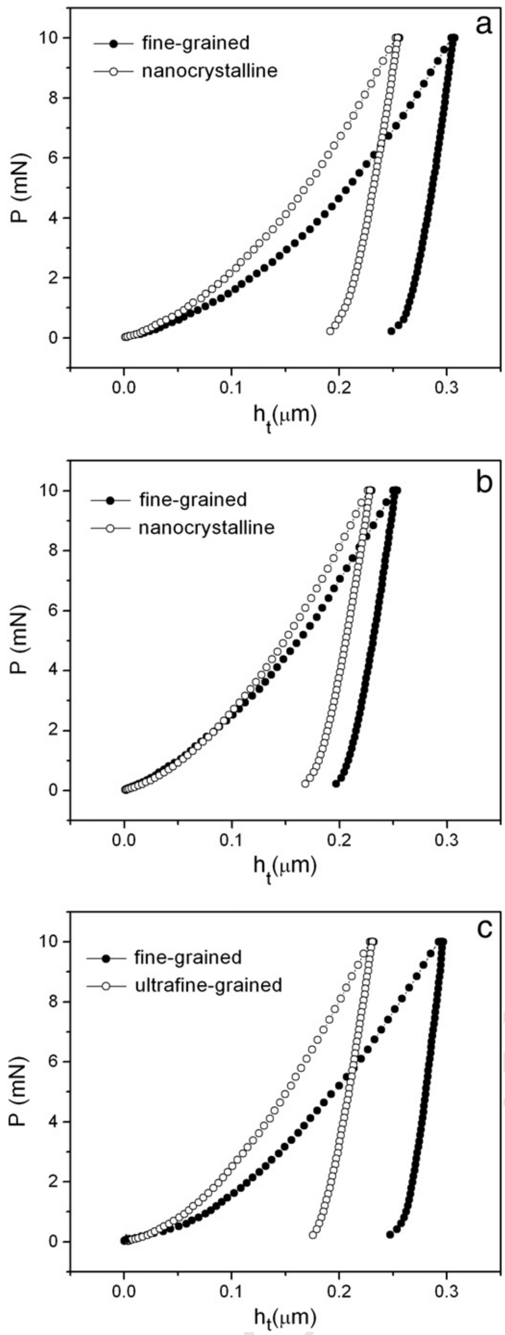

Fig. 6. Representative load–unload nanoindentation curves for (a) fine-grained $Cu_{0.57}Ni_{0.43}$ and nanocrystalline $Cu_{0.55}Ni_{0.45}$, (b) fine-grained $Cu_{0.14}Ni_{0.86}$ and nanocrystalline $Cu_{0.13}Ni_{0.87}$ and (c) fine-grained and ultrafine-grained pure Ni films.

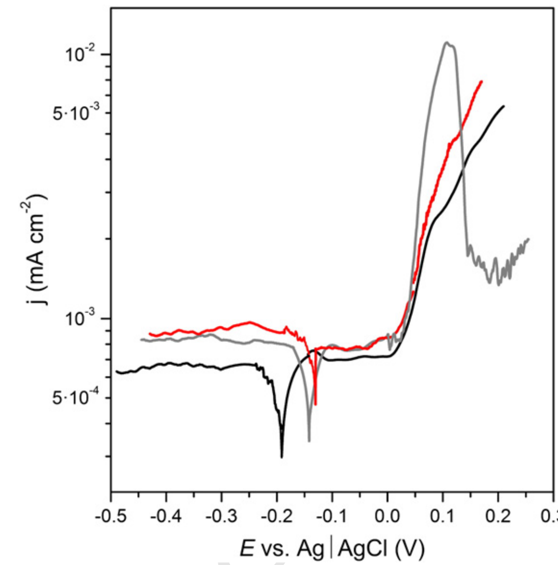

Fig. 7. Representative potentiodynamic polarisation curves of ultrafine-grained Ni (red curve), fine-grained $Cu_{0.14}Ni_{0.86}$ (grey curve) and nanocrystalline $Cu_{0.13}Ni_{0.87}$ (black curve) films onto Cu/Ti/Si (100) substrates. (For interpretation of the references to colour in this figure legend, the reader is referred to the web version of this article.)

Mohan observed $E_{corr} = -0.245$ V vs. saturated calomel electrode (SCE) (i.e. −0.208 V vs. Ag|AgCl (3.5 M KCl)) in Ni-rich Cu–Ni films (15–50 nm crystallite size) brush plated onto copper substrate [71]. This value is close to the E_{corr} observed for nanocrystalline $Cu_{0.13}Ni_{0.87}$ films electroplated. However, further Cu alloying did not seem to improve corrosion resistance, despite its higher nobility. Based on the electron configuration theory of passivity [72], it has been claimed that passive films formed on alloys with a Cu/Ni atomic ratio exceeding 1.6 are less stable [73].

One would intuitively expect corrosion to be initiated more easily at defects sites (e.g. grain boundaries and triple junctions in nanocrystalline metals). For a given Cu–Ni composition, nanostructuring caused a noticeable shift of E_{corr} towards more negative values, but resulted in a decrease in j_{corr}. These results are in agreement with the work by Troyon et al., where it is reported that Ni/Cu multilayers prepared with saccharine showed more negative E_{corr} values but lower j_{corr} than the multilayers prepared without saccharine (i.e. with larger grain sizes) in 3.0 wt.% NaCl solution [74]. Similarly, the corrosion rate in 1 M H_2SO_4 solution was also found to decrease in nanocrystalline Ni films electroplated from a saccharine-containing Watt's bath when the grain size was lowered from 28 to 8 nm [75]. Due to the role of saccharine as a sulphur source, the inclusion of low amounts of sulphur in the nanocrystalline $Cu_{1-x}Ni_x$ films cannot be ruled out, and, as observed in other alloys, is partly responsible for the negative shift in E_{corr} [76].

Table 3
Hardness (*H*), reduced Young's modulus (E_r) and H/E_r, H^3/E_r^2 and W_{el}/W_{tot} ratios extracted from the corresponding indentation curves of the listed thin films. W_{el} and W_{tot} denote the elastic and total indentation energies, respectively.

Film	*H* (GPa)	E_r (GPa)	H/E_r	H^3/E_r^2 (GPa)	W_{el}/W_{tot} (%)
Fine-grained $Cu_{0.57}Ni_{0.43}$	4.2 ± 0.4	164 ± 4	0.0256 ± 0.0016	0.0027 ± 0.0012	19.2 ± 0.7
Nanocrystalline $Cu_{0.55}Ni_{0.45}$	6.7 ± 0.2	172 ± 3	0.0389 ± 0.0012	0.0102 ± 0.0008	27.1 ± 0.5
Fine-grained $Cu_{0.14}Ni_{0.86}$	5.4 ± 0.3	195 ± 3	0.0277 ± 0.0015	0.0041 ± 0.0010	20.1 ± 0.6
Nanocrystalline $Cu_{0.13}Ni_{0.87}$	8.2 ± 0.2	192 ± 3	0.0427 ± 0.0012	0.0149 ± 0.0008	30.2 ± 0.5
Fine-grained Ni	4.3 ± 0.3	196 ± 3	0.0219 ± 0.0015	0.0021 ± 0.0010	14.7 ± 0.6
Ultrafine-grained Ni	8.0 ± 0.2	193 ± 3	0.0415 ± 0.0012	0.0137 ± 0.0008	29.5 ± 0.5

Please cite this article as: E. Pellicer, et al., Surf. Coat. Technol. (2011), doi:10.1016/j.surfcoat.2011.05.047

Table 4
Corrosion data obtained from the polarisation experiments in aerated 3.5 wt.% NaCl.

Film	E_{corr} (V)	j_{corr} (μA cm^{-2})	Active–passive transition
Fine-grained $Cu_{0.57}Ni_{0.43}$	−0.163	6.3	yes
Nanocrystalline $Cu_{0.55}Ni_{0.45}$	−0.200	5.8	yes
Fine-grained $Cu_{0.14}Ni_{0.86}$	−0.140	6.5	yes
Nanocrystalline $Cu_{0.13}Ni_{0.87}$	−0.197	5.8	no
Ultrafine-grained Ni	−0.131	7.7	no

Nanostructured materials prepared by mechanical methods are usually characterised by a large number of pores and microstrains, which are particularly susceptible to corrosion. Electrodeposition is known to provide dense and pore-free nanostructured metals, which make them less prone to certain types of corrosion such as pitting [77]. In addition, the compact morphology and even surface of the nanocrystalline Cu–Ni alloys prepared help in lowering the dissolution rate, whereas the edged morphology of the fine-grained films allow an easier access of corrosive species (i.e. Cl^{-}) to the film/substrate interface. From the application point of view, the tradeoff between E_{corr} and j_{corr}, makes the nanocrystalline Cu–Ni films good candidates for protective coatings in marine environments.

4. Conclusions

In situ formation of both fine-grained or nanocrystalline Cu–Ni films with variable composition was made possible by electrodeposition. The effects of a saccharine-assisted nanostructuring process on the morphology, structure, mechanical and corrosion properties of Cu–Ni films plated galvanostatically on silicon-based substrates have been discussed. Smooth films featuring much smaller crystallite sizes, lower microstrain, and larger numbers of stacking faults were obtained from saccharine-containing baths. The nanocrystalline films showed improved mechanical properties (larger hardness and elastic recovery and better wear resistance) compared to fine-grained films, whilst retaining good corrosion resistance in a chloride medium. These attributes surpassed those of pure Ni films obtained from a similar electrolytic bath. The present study clearly demonstrates that nanostructuring improves the properties of Cu–Ni alloys and thereby enables a wider range of applications for this system.

Acknowledgements

The authors wish to thank the Servei de Microscòpia of the Universitat Autònoma de Barcelona for the technical assistance during TEM characterisation. This work has been partially financed by the 2009-SGR-1292 and MAT2007-61629 research projects. E.P. is indebted to the DURSI of the Generalitat de Catalunya for the Beatriu de Pinós postdoctoral fellowship. S.P. acknowledges a postdoctoral fellowship of Spanish MICINN. M.D.B. was partially supported by an ICREA ACADEMIA award.

References

[1] K. Lu, L. Lu, S. Suresh, Science 324 (2009) 349.
[2] M. Chen, E. Ma, K.J. Hemker, H. Sheng, Y. Wang, X. Cheng, Science 23 (2003) 1275.
[3] L. Lu, M.L. Sui, K. Lu, Science 25 (2000) 1463.
[4] K.S. Kumar, S. Suresh, M.F. Chisholm, J.A. Horton, P. Wang, Acta Mater. 51 (2003) 387.
[5] K.S. Kumar, H. Van Swygenhoven, S. Suresh, Acta Mater. 51 (2003) 5743.
[6] M. Dao, L. Lu, R.J. Asaro, J.T.M. De Hosson, E. Ma, Acta Mater. 55 (2007) 4041.
[7] C.C. Koch, K.M. Youssef, R.O. Scattergood, K.L. Murty, Adv. Eng. Mater. 7 (2005) 787.
[8] H. Gleiter, Prog. Mater. Sci. 33 (1989) 223.
[9] A. Boé, A. Safi, M. Coulombier, D. Fabrègue, T. Pardoen, J.-P. Raskin, Smart Mater. Struct. 18 (2009) 115018.
[10] T.M. Manhabosco, I.L. Müller, Surf. Coat. Technol. 202 (2008) 3585.
[11] B. Subramanian, S. Mohan, S. Jayakrishnan, M. Jayachandran, Curr. Appl. Phys. 7 (2007) 305.
[12] S. Tao, D.Y. Li, Nanotechnol. 17 (2006) 65.
[13] F. Wang, K. Hosoiri, S. Doi, N. Okamoto, T. Totsuka, T. Watanabe, Electrochem. Commun. 6 (2004) 1149.
[14] D.-Y. Park, R.Y. Song, J.M. Ko, B.Y. Yoo, N.V. Myung, Electrochem. Sol. State Lett. 8 (2005) C23.
[15] M. Klimenkov, A.S.M.A. Haseeb, K. Bade, Thin Solid Films 517 (2009) 6593.
[16] Y. Zhang, D.G. Ivey, Chem. Mater. 16 (2004) 1189.
[17] J.K. Dennis, J.J. Fuggle, Electroplat. Met. Finish. 21 (1968) 16.
[18] Á. Cziráki, B. Fogarassy, I. Geröcs, E. Tóth-Kádár, I. Bakonyi, J. Mater. Sci. 29 (1994) 4771.
[19] H. Natter, M. Schmelzer, R. Hempelmann, J. Mater. Res. 13 (1998) 1186.
[20] N.S. Qu, D. Zhu, K.C. Chan, W.N. Lei, Surf. Coat. Technol. 168 (2003) 123.
[21] Y.F. Shen, W.Y. Xue, Y.D. Wang, Z.Y. Liu, L. Zuo, Surf. Coat. Technol. 202 (2008) 5140.
[22] F. Sansoz, K.D. Stevenson, R. Govinthasamy, N.S. Murthy, Scr. Mater. 59 (2008) 103.
[23] Y. Pan, S. Jiang, C.-Y. Dai, T. Tang, Z.-F. Zhou, Y.-C. Zhou, Trans. Nonferrous Met. Soc. China 17 (2007) s770.
[24] A.M. Rashidi, A. Amadeh, Surf. Coat. Technol. 202 (2008) 3772.
[25] B.S.B. Reddy, K. Das, A.K. Datta, S. Das, Nanotechnol. 19 (2008) 115603.
[26] A.M. Rashidi, A. Amadeh, Surf. Coat. Technol. 204 (2009) 353.
[27] E. Gómez, E. Pellicer, E. Vallés, Electrochem. Commun. 6 (2004) 853.
[28] Sh. Hassani, K. Raeissi, M.A. Golozar, J. Appl. Electrochem. 38 (2008) 689.
[29] S. Guan, B.J. Nelson, J. Magn. Magn. Mater. 292 (2005) 49.
[30] E.J. Podlaha, Ch. Bonhôte, D. Landolt, Electrochim. Acta 39 (1994) 2649.
[31] T.A. Green, A.E. Russel, S. Roy, J. Electrochem. Soc. 145 (1998) 875.
[32] A.M. Beccaria, Y.Z. Wang, G. Poggi, Surf. Interf. Anal. 21 (2004) 442.
[33] I.G. Casella, M. Gatta, J. Electrochem. Soc. 149 (2002) B465.
[34] E. Pellicer, A. Varea, S. Pané, B.J. Nelson, E. Menéndez, M. Estrader, S. Suriñach, M.D. Baró, J. Nogués, J. Sort, Adv. Funct. Mater. 20 (2010) 983.
[35] J. Crousier, A.-M. Beccaria, Werks. Korr. 41 (1990) 185.
[36] I. Milošev, M. Metikoš-Huković, Electrochim. Acta 42 (1997) 1537.
[37] W.A. Badawy, K.M. Ismail, A.M. Fathi, J. Appl. Electrochem. 35 (2005) 879.
[38] M. Metikoš-Huković, I. Škugor, Z. Grubač, R. Babić, Electrohim. Acta 55 (2010) 3123.
[39] S.J. Bull, J. Phys. D-Appl. Phys. 38 (2005) R393.
[40] R.A. Young (Ed.), The Rietveld Method, Union of Crystallography, Oxford University Press, Oxford, 1995.
[41] L. Lutterotti, P. Scardi, J. Appl. Crystallogr. 23 (1990) 246.
[42] M. Morales, D. Chateigner, L. Lutterotti, Thin Solid Films 517 (2009) 6264.
[43] B.E. Warren, X-ray Diffraction, Addison-Wesley, Reading, MA/Dover, Mineola NY, 1969.
[44] A.C. Fischer-Cripps, in: F.F. Ling (Ed.), Nanoindentation, Springer, New York, 2004.
[45] W.C. Oliver, G.M. Pharr, J. Mater. Res. 7 (1992) 1564.
[46] Y. Nakamura, N. Kaneko, M. Watanabe, H. Nezu, J. Appl. Electrochem. 24 (1994) 227.
[47] E. Moti', M.H. Shariat, M.E. Bahrololoom, J. Appl. Electrochem. 38 (2008) 605.
[48] D. Mockute, G. Bernotiene, R. Vilkaite, Surf. Coat. Technol. 160 (2002) 152.
[49] U.S. Mohanty, B.C. Tripathy, S.C. Das, P. Singh, V.N. Misra, Hydrometallurgy 100 (2009) 60.
[50] S. Rode, C. Henninot, C. Vallières, M. Matlosz, J. Electrochem. Soc. 151 (2004) C405.
[51] S. Rode, C. Henninot, M. Matlosz, J. Electrochem. Soc. 152 (2005) C248.
[52] X. Cui, W. Chen, J. Electrochem. Soc. 155 (2008) K133.
[53] R. Weil, Annu. Rev. Mater. Sci. 19 (1989) 165.
[54] A. Bhandari, S.J. Hearne, B.W. Sheldon, S.K. Soni, J. Electrochem. Soc. 156 (2009) D279.
[55] L. Lu, Y. Shen, X. Chen, L. Qian, K. Lu, Science 304 (2004) 422.
[56] T.A. Tochitskii, A.E. Dmitrieva, Russ. J. Electrochem. 39 (2003) 305.
[57] V. Velinov, S. Vitkova, N. Pangarov, Surf. Coat. Technol. 6 (1977) 19.
[58] V. Randle, Acta Mater. 47 (1999) 4187.
[59] J. Wong, W.E. Nixon, J.W. Mitchell, S.S. Laderman, J. Appl. Phys. 71 (1992) 150.
[60] J.R. Davis (Ed.), Nickel, Cobalt, and their Alloys, ASM International, USA, 2000, p. 4.
[61] http://www.nickel-alloys.net/index.html.
[62] G.F. Wang, X.Q. Feng, S.W. Yu, Chin. Sci. Bull. 47 (2002) 1493.
[63] P.G. Sanders, J.A. Eastman, J.R. Weertman, Acta Mater. 45 (1997) 4019.
[64] G.E. Fougere, L. Riester, M. Ferber, Mater. Sci. Eng. A 204 (1995) 1.
[65] H.S. Kim, M.B. Bush, Nanostruc. Mater. 11 (1999) 361.
[66] M. Legros, B.R. Elliott, M.N. Rittner, Philos. Mag. A 80 (2000) 1017.
[67] A. Leyland, A. Matthews, Wear 246 (2000) 1.
[68] J. Musil, F. Kunc, H. Zeman, H. Poláková, Surf. Coat. Technol. 154 (2002) 304.
[69] P.H. Mayrhofer, C. Mitterer, J. Musil, Surf. Coat. Technol. 177–178 (2004) 725.
[70] E.A. Levashov, D.V. Shtansky, Russ. Chem. Rev. 76 (2007) 463.
[71] N. Rajasekaran, S. Mohan, J. Appl. Electrochem. 39 (2009) 1911.
[72] H.H. Uhlig, Z. Elektrochem. 62 (1958) 700.
[73] F. Mansfeld, H.H. Uhlig, Corr. Sci. 9 (1969) 377.
[74] M. Troyon, L. Wang, Appl. Surf. Sci. 103 (1996) 517.
[75] R. Mishra, R. Balasubramaniam, Corr. Sci. 46 (2004) 3019.
[76] J. George, J. Rantschler, S.-E. Bae, D. Litvinov, S.R. Brankovic, J. Electrochem. Soc. 155 (2008) D589.
[77] S.K. Ghosh, G.K. Dey, R.O. Dusane, A.K. Grover, J. Alloy Comp. 426 (2006) 235.

Please cite this article as: E. Pellicer, et al., Surf. Coat. Technol. (2011), doi:10.1016/j.surfcoat.2011.05.047